

Analysis on the full scale measurement data of 9400TEU container Carrier with hydroelastic response



Yooil Kim^{a,*}, Byung-Hoon Kim^a, Byung-Ki Choi^b, Sung-Gun Park^c, Sime Malenica^d

^a Department of Naval Architecture and Ocean Engineering, INHA University, 100, Inha-ro, Nam-gu, Incheon, South Korea

^b Marine Structure Research Department, Hyundai Heavy Industries, Co., Ltd, 1000, Bangeojinsunhwando, Dong-gu, Ulsan, South Korea

^c DSME R&D Institute, Daewoo Shipbuilding and Marine Engineering, Co., Ltd, 3370, Geaje-daero, Geoje-si, Gyeongsangnam-do, South Korea

^d Research Department, Marine & Offshore Division, Bureau Veritas, 92200, Neuilly sur Seine, France

ARTICLE INFO

Keywords:

Hydroelasticity
Natural frequency
Damping ratio
Random decrement technique
Proper orthogonal decomposition
Fatigue

ABSTRACT

Since the advent of hydroelasticity issues in the marine community, a full scale measurement campaign has been considered the most important research to reach a thorough understanding of this complicated physical phenomenon. This study examined the full-scale measurement data of a large container carrier with a 9400TEU capacity. First, modal parameters, such as the mode shapes, natural frequencies, and damping ratios, were examined based upon the measured acceleration data on deck. The evolution of the natural frequencies and damping ratios were also checked and their correlation was explored. In addition, the modal magnitude obtained using the acceleration data was cross-compared with the strain at deck to investigate their temporal relevance. Finally, the fatigue damage was calculated using the measured strain at deck and the expected long-term fatigue damage was estimated based upon the fatigue damage experienced by the vessel during the measurement period.

1. Introduction

Hydroelasticity is recognized as one of the main challenges in the design of modern merchant ships, such as ultra large container carriers and very large ore carriers. Hydroelasticity refers to either the resonant vibratory response of a flexible ship structure under a random ocean wave load, or transient vibratory response induced by an impulsive slamming load that takes place when the ship plunges into the free surface with waves. The former is called springing and the latter is called whipping. The importance of hydroelasticity has become of prime importance since the advent of larger and faster ships, which has increased dramatically the likelihood of resonance between the ship structure and an incoming wave as well as transient vibrations due to the flexibility of the ship.

Considerable research efforts are currently focused on the hydroelasticity problem to establish a robust design methodology, ultimately targeting the safe operation of unprecedentedly large ships. On the other hand, this goal has yet to be achieved owing to the inherent nonlinear nature of the physics behind the hydroelasticity. Some numerical methodologies have been developed under a linear or weakly nonlinear assumption in both the time and frequency domains, the majority of which are based on the combination of potential theory and the finite element method (Price and Temarel, 1982, Jensen and Doglioni, 1996, Wu and Moan, 1996, Malenica et al., 2003, Hirdaris et al., 2003, Kim, 2009, Kim et al., 2013). Computational fluid dynamics coupled with finite element methods is a potentially powerful numerical methodology to solve the problem considering any type of nonlinearity. The model basin

* Corresponding author.

E-mail addresses: yooilkim@inha.ac.kr (Y. Kim), kbh0517hoon@hanmail.net (B.-H. Kim), bkchoi@hhi.co.kr (B.-K. Choi), sgpark8@dsme.co.kr (S.-G. Park), sime.malenica@bureauveritas.com (S. Malenica).

test with either a segmented hull model or flexible model is another powerful way to examine the hydroelasticity problem. Many model basin tests have been carried out recently, the majority of which were based on the segmented hull model targeting the vibratory behavior of the hull under wave loads [1–5]. Some full scale measurement campaigns have been carried out for large commercial ships, such as bulk/ore carriers and large container carriers [6–9]. The results showed that the vertical bending moment was increased by several tens of percent due to the whipping effect, and both springing and whipping tended to increase the fatigue damage through continuous global hull girder vibrations [11]. Investigated the influence of springing and whipping on both fatigue and extreme loading of container carrier via full scale measurement and model basin test. It was found that whipping increases the fatigue damage and extreme loading considerably and has to be taken into account with similar importance as quasi-static wave loading.

Modal parameter estimation of a dynamically vibrating structure, particularly using operational modal analysis, is an interesting research topic that has attracted considerable attention in many engineering fields. Operational modal analysis is an emerging technology through which unknown modal parameters can be estimated using the output data only. Among these, proper orthogonal decomposition (POD) and the random decrement technique (RDT) are commonly used signal processing techniques for identifying the modal parameters, such as mode shapes, natural frequencies, and damping ratios. POD is an order reduction technique through which the motion of a dynamic system with a large DOF can be represented by the superposition of a few basic modes. The idea comes from the fact that the eigenvector of a spatial coherence matrix of time varying physical quantities measured at different locations is the mode shapes of the dynamic system under consideration [12]. First applied the method to analyze the spatial distribution characteristics of turbulence in a fluid field, and later extended to the extraction of the mode shapes of a vibrating structure [13,14]. RDT is another interesting technique that can be used to extract some modal parameters [15,16]. Originally developed the technique in the form of an ‘auto’ random decrement to identify the dynamic characteristics and detect in-service damage of the space structure from the measured response only [17]. Later introduced the concept of the cross random decrement that enabled an identification of the mode shapes of a multi-DOF system.

Previous studies focused on the modal parameter estimation of a hydroelastically responding ship structure using operational modal analysis, mainly with the model basin test results [18]. Applied the POD method to identify the mode shapes of a segmented hull model made of a flexible backbone connecting separate hull segments. The first, second, and third vertical mode shapes were estimated by processing both the measured vertical bending moment (VBM) and acceleration using the POD, and both results showed good agreement with each other [19]. Applied the random decrement technique together with a wavelet transform to identify the modal parameters of a flexible seagoing vessel. They reported that the damping ratio under wet towing conditions was approximately 20% larger than that obtained by the wet hammering test [20]. Applied the proper orthogonal decomposition method and cross random decrement technique to extract the mode shapes of a segmented ship model of a 400 K ore carrier. The vertical bending modes of the 2 and 3 node vibration were clearly captured and the correspondence between the two results was quite good.

In the present study, the dynamic modal parameters were extracted by analyzing the full scale measurement data of a 9400TEU container carrier. The modal parameters, such as mode shapes, natural frequencies and damping ratios, were estimated by processing the acceleration signals measured on 10 separate locations on deck along the ship length. In addition, the temporal evolution of the natural frequencies and damping ratios were checked and their correlation was examined to check the relevance between them. Correlation analyses were also performed to check the relevance of the extracted modal magnitude and the strain on deck. Finally, the fatigue damage was estimated for a typical artificial structural detail on the deck of the vessel using the measured strain, and the fatigue damage of the cases with and without vibration were compared.

2. Methodologies

2.1. Band-pass filter

A band-pass filter is a technique that filters out signals of other frequency bands while leaving only the signals of a specific frequency band, and is applied widely to the filtering of signals. Fig. 1 presents a schematic diagram of the shape and parameters of the band-pass filter expressed in the frequency domain.

If there is an overlap of energy concentration between the neighboring vibration modes, the filter is generally designed in such a way that a sloping region at both ends of the filter bank are arranged to properly decompose the energy within the overlapping frequency region. The band-pass filter is expressed in the frequency domain as Eq.(1):

$$H(\omega) = \begin{cases} 0 \text{ to } 1, & \omega_c - \Delta\omega_t - \Delta\omega_s \leq \omega < \omega_c - \Delta\omega_t \\ 1, & \omega_c - \Delta\omega_t \leq \omega < \omega_c + \Delta\omega_t \\ 1 \text{ to } 0, & \omega_c + \Delta\omega_t \leq \omega < \omega_c + \Delta\omega_t + \Delta\omega_s \end{cases} \quad (1)$$

To filter a given signal, $f(t)$, with the band-pass filter of Eq. (1), the given signal, $f(t)$, is subjected to a Fourier transform and is windowed by the designed filter, $H(\omega)$, as shown in Eq.(2). The filtered time series is then obtained by an inverse Fourier transform.

$$\tilde{f}(t) = \int_{-\infty}^{\infty} F(\omega) H(\omega) e^{i\omega t} d\omega \quad (2)$$

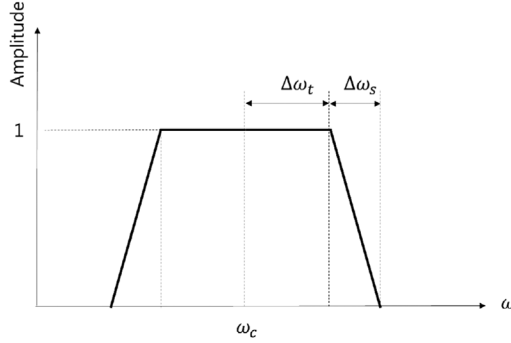


Fig. 1. Band-pass filter and its parameters.

2.2. Proper orthogonal decomposition

The POD starts with the spatial coherence matrix of a certain physical quantity, such as torsional moment, VBM at different locations along the ship length in this particular case. The ensemble matrix of the measured sectional loads at M different locations along the ship is defined in Eq.(3):

$$\mathbf{X} = [\mathbf{x}_1, \mathbf{x}_2, \mathbf{x}_3, \dots, \mathbf{x}_M]. \quad (3)$$

where the column vector, \mathbf{x}_i , stands for the sectional load time history of N discrete time intervals, and can be represented by Eq.(4):

$$\mathbf{x}_i = [x_i(t_1), x_i(t_2), x_i(t_3), \dots, x_i(t_N)]^T. \quad (4)$$

The time histories of the sectional load may be assumed to be a linear combination of the normal modes as follows:

$$\mathbf{x}(t) = e_1(t)\mathbf{v}_1 + e_2(t)\mathbf{v}_2 + \dots + e_M(t)\mathbf{v}_M, \quad (5)$$

where $e_i(t)$ is the time modulation of the i th mode. The ensemble matrix given in Eq. (3) has the form,

$$\mathbf{X} = [\mathbf{x}(t_1), \mathbf{x}(t_2), \dots, \mathbf{x}(t_N)]^T = [\mathbf{e}_1\mathbf{v}_1^T + \mathbf{e}_2\mathbf{v}_2^T + \dots + \mathbf{e}_M\mathbf{v}_M^T], \quad (6)$$

where the row vector \mathbf{e}_i is defined as $[e_i(t_1), e_i(t_2), \dots, e_i(t_N)]$. The spatial coherence matrix post multiplied by \mathbf{v}_j gives,

$$\mathbf{R}\mathbf{v}_j = \frac{1}{N}\mathbf{X}^T\mathbf{X}\mathbf{v}_j = \frac{1}{N}[\mathbf{e}_1\mathbf{v}_1^T + \mathbf{e}_2\mathbf{v}_2^T + \dots + \mathbf{e}_M\mathbf{v}_M^T]^T[\mathbf{e}_1\mathbf{v}_1^T + \mathbf{e}_2\mathbf{v}_2^T + \dots + \mathbf{e}_M\mathbf{v}_M^T]\mathbf{v}_j, \quad (7)$$

where the matrix, \mathbf{R} , is defined as a spatial coherence matrix, i.e., $\frac{1}{N}\mathbf{X}^T\mathbf{X}$. Each entry of the coherence matrix, R_{ij} , is the inner product of the two measured VBM time histories at locations i and j , which indicates the correlation of the VBM of the two locations. Considering the orthonormality of the eigenvectors, the far right term of Eq.(7) becomes

$$\mathbf{R}\mathbf{v}_j = \frac{1}{N}(\mathbf{v}_1\mathbf{e}_1^T\mathbf{e}_j + \mathbf{v}_2\mathbf{e}_2^T\mathbf{e}_j + \dots + \mathbf{v}_M\mathbf{e}_M^T\mathbf{e}_j). \quad (8)$$

All terms of Eq.(8) except for $\mathbf{v}_i\mathbf{e}_i^T\mathbf{e}_j$ will disappear because of the distinct frequency of each vibration mode when the signal record length is long enough. Hence,

$$\lim_{N \rightarrow \infty} \frac{1}{N}\mathbf{v}_i\mathbf{e}_i^T\mathbf{e}_j = 0 \quad \text{when } i \neq j. \quad (9)$$

Taking advantage of Eq.(9), Eq.(8) finally becomes

$$\mathbf{R}\mathbf{v}_j = \frac{\mathbf{e}_j^T\mathbf{e}_j}{N}\mathbf{v}_j = \lambda\mathbf{v}_j. \quad (10)$$

Eq.(10) implies that the eigenvectors of the coherence matrix, \mathbf{R} , which is called the proper orthogonal mode (POM), become the modal vector of the given system that the measurement is based on. Eq.(6) holds only when the external excitation is absent, i.e., the free vibration case, but most real world situations are forced vibrations. If the external harmonic excitation is present, different mode shapes may be excited with the same frequency so that Eq.(9) will no longer hold. Nevertheless, if one of the modes resonates with a predominantly large magnitude, the POM becomes a good approximation of the mode shape. The accuracy of the approximation depends strongly on the relative magnitude of the resonant and non-resonant vibration. The hydroelastic response of a flexible ship is a vibration near the natural frequency with relatively small damping, which can be confirmed in the frequency domain with sharp peaks right on the natural frequency of the system. Therefore, the derived POMs based on Eq.(10) is a good approximation of the mode shapes of a vibrating ship structure.

2.3. Random decrement technique

The random decrement technique is a simple but very powerful method for identifying a dynamic system. This technique is used widely for modal parameter identification, where prior information on excitation is unknown. Assuming that the signals, $x(t)$ and $y(t)$, represent the VBM at two different locations along the ship length, the auto and cross random decrement signature is defined as the expected value of the given signal $x(t)$ under certain conditions, which are denoted as $T_{x(t)}$.

$$D_{xx}(\tau) = E[x(t + \tau)|T_{x(t)}] D_{xy}(\tau) = E[y(t + \tau)|T_{x(t)}] \quad (11)$$

$D_{xx}(\tau)$ is the auto random decrement signature and $D_{xy}(\tau)$ is the cross random decrement signature, and they both become the free decay signal at two different locations, x and y . The idea behind Eq.(11) is to cancel out the particular solution of the dynamic response of a given system by taking the conditional average across a large number of ensembles, leaving the homogeneous solution to be averaged. While taking the average across the ensembles, a certain condition is imposed so that the cancellation can be achieved using a finite number of ensembles.

Assuming that the process is ergodic, which means the stationarity of the process, Eq.(11) can be rewritten as Eq.(12). Therefore, conditional averaging across the ensembles can be made within a single sample realization.

$$D_{xx}(\tau) = \frac{1}{N} \sum_{i=1}^N x(t_i + \tau)|T_{x(t_i)} D_{xy}(\tau) = \frac{1}{N} \sum_{i=1}^N y(t_i + \tau)|T_{x(t_i)} \quad (12)$$

where N is the number of points in the random process that satisfy the condition, $T_{x(t)}$. The condition, $T_{x(t)}$, under which the mean values of $x(t)$ and $y(t)$ are taken, is called the triggering condition. This condition can be divided into several different types, such as level crossing triggering, local extremum triggering, positive point triggering, and zero crossing triggering. In this study, the level crossing-triggering condition was applied to extract the free decay signal from the measured one, and it can be rewritten in a general form as Eq.(13).

$$T_{x(t)}^T = \{-a \leq x(t) < a + \Delta a, 0 \leq \dot{x}(t) < \infty\} \quad (13)$$

where Δa is the triggering range, which was set to be infinitesimally small.

3. Target ship and measurement system

3.1. Main particulars

The dynamic characteristics of a ship responding to an incoming wave were studied by analyzing the full scale measurement data of Rigoletto, a container ship owned by CMA-CGM. Table 1 lists Rigoletto's main specifications.

3.2. Acceleration measurement

A total of eleven accelerometers were arranged to the Rigoletto and the translational acceleration in the x , y , and z directions at each location were measured. The measurement unit is m/s^2 , and Fig. 2 shows the position of the accelerometer.

Accelerometers were installed at the deck passage ways of both port and starboard (Fr 13, 74, 102, 124), the forward frame structure (Fr 154), and wheelhouse. The local x axis of the accelerometer coincides with the x axis of the ship's fixed coordinate system, which points from the stern to bow, except for the sensors installed in the forward frame structure, in which case, the local x axis is oriented vertically downward. The accelerometer installed on the forward frame structure was installed so that the direction of the local z -axis coincides with the negative of the global y -axis. Table 2 lists the relative orientation of the accelerometer and the z -axis local coordinates.

3.3. Strain measurement

A total of 10 long base strain gauges (LBSG) were attached to the vessel and the strain at each location was measured with a sampling frequency of 20 Hz. The measurement unit of the strain data was mA and was stored in the data file in micro strain [m/m] after being multiplied by a sensitivity value of 312.5 micro strain [m/m]/mA. Fig. 3 shows the location of the LBSG.

Six LBSGs were installed at Fr. 75(Cargo hold 8, H8), which corresponds to the afterward 25% of the ship length, and 4 LBSGs were installed at Fr. 100(Cargo hold 6, H6), corresponding to the afterward 50% of the ship length. Fig. 4 shows the detail locations of the LBSGs in cargo hold 8. The LBSG installed between longitudinal 38 and 40 of cargo hold 8 with a 45° inclination angle aims to measure the shear strain near the neutral axis of the ship.

4. Signal preprocessing

The original signal was preprocessed properly to remove the potential drift and unphysical oscillation in high frequencies. As shown in Fig. 5, the drift of the LBSG signal was so high that removing the drift is a very important task to guarantee the validity of the signal itself.

Table 1
Main specifications of CMA-CGM Rigoletto.

Vessel name	CMA CGM Rigoletto
Operator	CMA CGM
Owner	CMA CGM
Flag/Nationality	France
Completion year	2006
Shipyard	Hyundai HI Ltd. Co, South Korea
Engine design	B&W
Power output	68666
Maximum speed	25.4
Overall length	350.00
Overall beam	42.80
Maximum draft	14.50
Maximum TEU capacity	9415
Reefer container	700
Dead weight	108000
Gross tonnage	99500

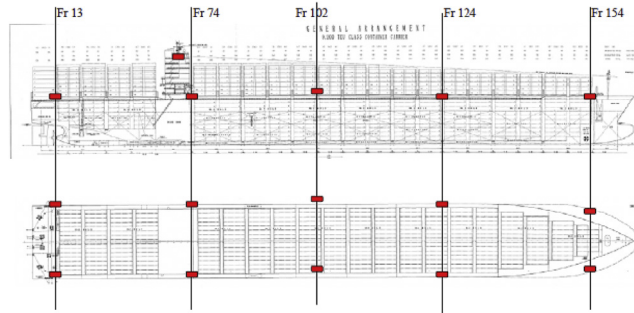


Fig. 2. Accelerometer arrangement on the ship.

Table 2
Accelerometer positions.

Sensor	Name	X	Y	Z	Sensor local z direction	
S1	SB frame 13	9.60	-19.25	25.70	0	0
S2	SB frame 74	86.80	-19.25	25.70	0	0
S3	SB frame 102	167.30	-19.25	25.70	0	0
S4	SB frame 128	231.60	-19.25	25.70	0	0
S5	SB frame 154	319.50	-19.25	25.70	0	-1
S6	SB frame 13	9.60	-19.25	25.70	0	0
S7	SB frame 74	86.80	-19.25	25.70	0	0
S8	SB frame 102	167.30	-19.25	25.70	0	0
S9	SB frame 128	231.60	-19.25	25.70	0	0
S10	SB frame 154	319.50	-19.25	25.70	0	1
S11	Wheel house	75.00	4.30	47.60	0	0

To remove the signal drift, the following procedure described in Fig. 6 below was used:

To filter the original raw data, a traditional low-pass filter scheme was employed with a cut-off frequency of 0.4 Hz, above which the vibration component exists. The smoothed signal was calculated using the moving regression filter, where the local quadratic function was used to smooth the original data within a certain interval. The local quadratic function about t_0 was assumed to be Eq. (14).

$$f(t) \approx \beta_0 + \beta_1(t - t_0) + \frac{1}{2}\beta_2(t - t_0)^2 \quad \text{for } t \in [t_0 - h_0(t_0), t_0 + h_0(t_0)] \quad (14)$$

The quadratic function defined as Eq.(14) covers the interval of t within $[t_0 - h_0(t_0), t_0 + h_0(t_0)]$ and the coefficients were determined using the weighted least square method. Eq.(15) shows how the parameter vector $\hat{\beta}$ is determined using the weighted least square method.

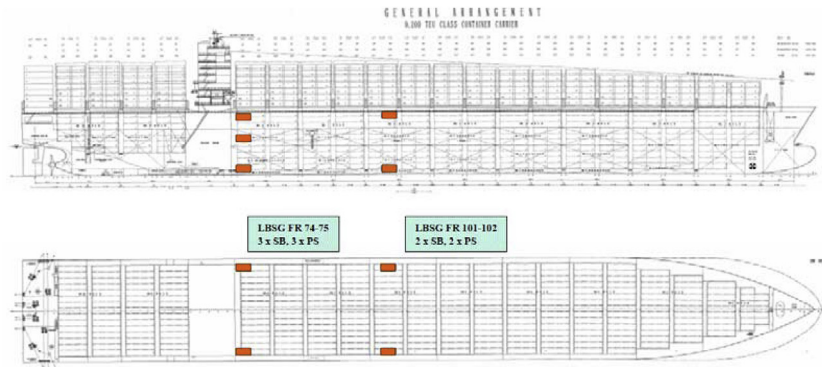


Fig. 3. Long base strain gauge arrangement.

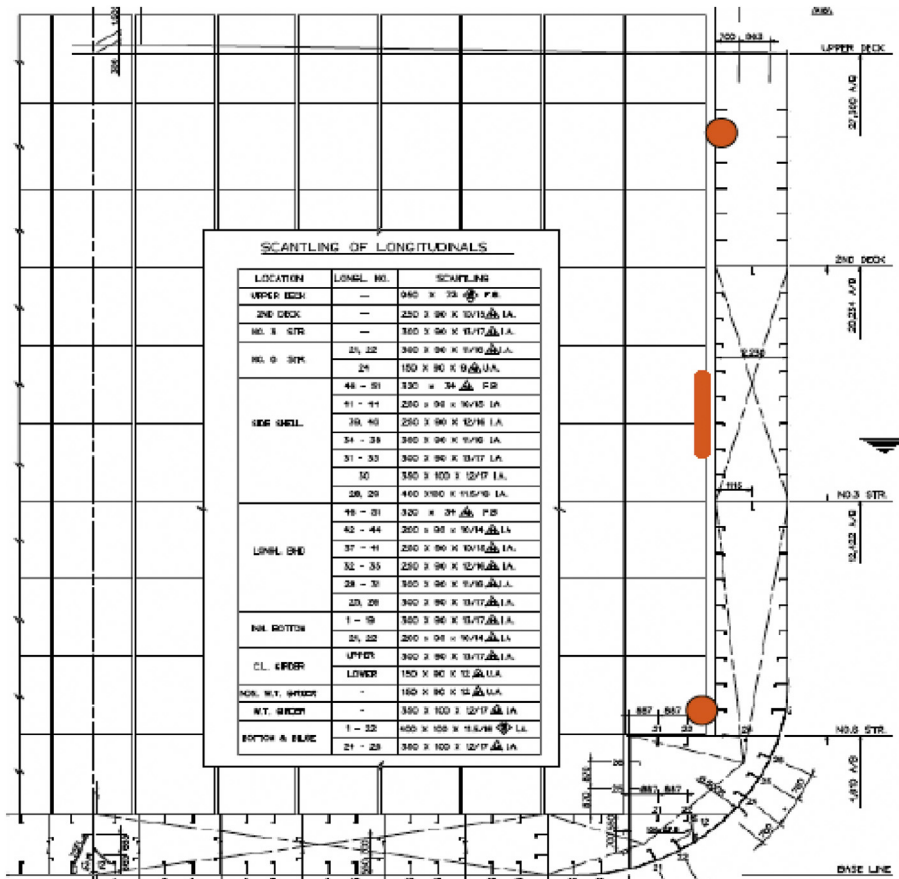


Fig. 4. Cross section of cargo hold 8 with the LBSG arrangement.

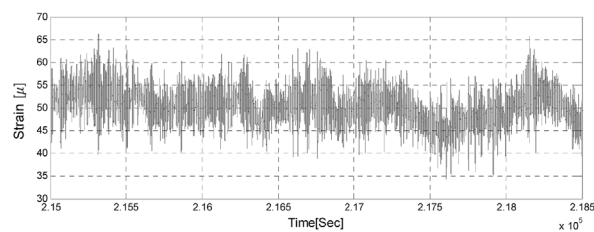
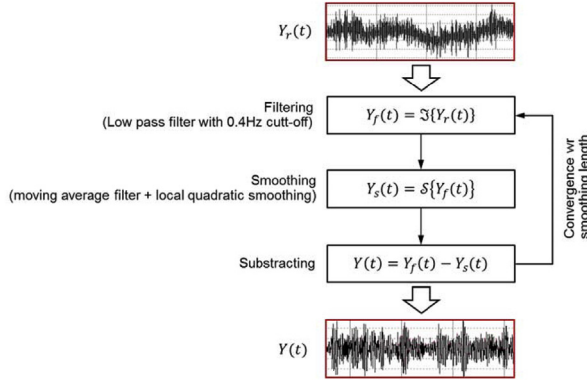


Fig. 5. Raw LBSG signal with drift.

**Fig. 6.** Procedure for drift removal.

$$\hat{\beta} = \text{average min} \left(\sum_{i=1}^n \omega_i(t_0) \left[y_{\text{filtered}}(t_i) - \left\{ \beta_0 + \beta_1(t_i - t_0) + \frac{1}{2}\beta_2(t_i - t_0)^2 \right\} \right]^2 \right) \quad (15)$$

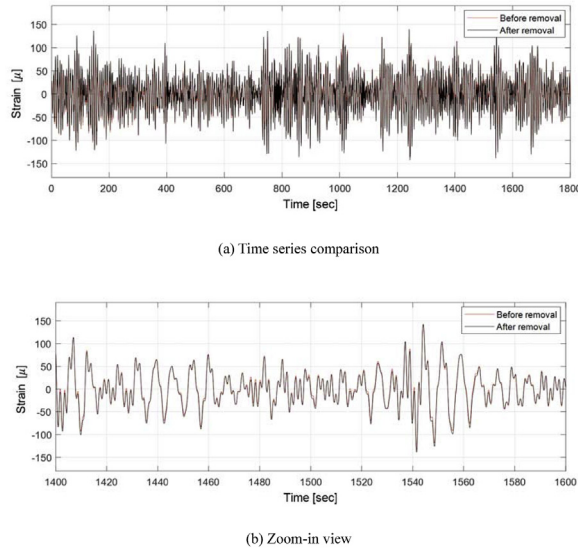
Because the drift, which is represented by $y_{\text{smooth}}(t)$, depends on the local smoothing length, some sensitivity study was performed to check the suitability of drift-removal. Three different local smoothing lengths, 5000, 2000 and 500, were tested and the quality of smoothing was checked via a time series comparison before and after drift removal. The local smoothing length of 500 time steps corresponded to 0.04 Hz, and was considered to be the upper bound of the drift frequency; hence, it was selected as the parameter.

Fig. 7 clearly shows that there is no drift in the raw LBSG signal, and that drift-removal did not influence the actual physical fluctuations when a local smoothing length of 500 was used. As mentioned above, this is a typical situation and is considered to be the case of most time-slots. Time-slot #179 shown in **Fig. 8** indicates considerable signal drift throughout the entire time span; however, it was removed successfully by the drift-removal method used in this study.

Unlike the LBSG data, which contains a significant slowly varying drift, the acceleration signal did not experience any considerable drift phenomenon, as shown in **Fig. 9**. Regarding the acceleration signal, no particular preprocessing work has been done except for the removal of the mean value.

5. Time-slot selection

The measured signal was logged into files with a time duration of 30 min. To avoid the situation that some unnecessary data are treated, the time-slots were selected out of a total measurement campaign period, which lasted for 9 months from August 5, 2007 to May 13, 2008. The standard deviation of the randomly fluctuating shear strain was used as a reference value to select the time-slots during which the vibration was considered to be significant. Two long-based strain gages were installed at both the port and starboard of the neutral axis of the vessel's midship with its inclination angle of 45°, so that the shear strain induced either by torsion or

**Fig. 7.** LBSG time history at portside of the mid-ship deck (Time-slot Nr. 120).

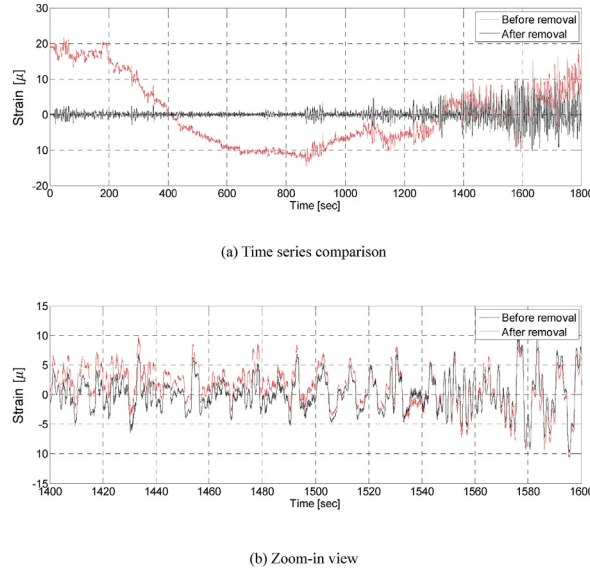


Fig. 8. LBSG time history at portside of the mid-ship deck (Time-slot Nr. 179).

vertical bending was captured.

Fig. 10(a) and (b) shows the time evolution of the standard deviation of the shear strain at both port and starboard. The horizontal axis is the identification number of the time-slots and the vertical axis is the standard deviation of the shear strain measured at the mid-height of the ship. The time-slots, whose standard deviations exceed 50% of the maximum case, were selected, as indicated by the red star marks in Fig. 10(a) and (b). The total number of selected time-slots was 207, which corresponds to the upper 2% of the entire time-slots.

6. Estimation of the mode shapes and damping ratios

6.1. Acceleration component decomposition

The analyses were done for the vertical bending and torsion vibration modes using the vertical acceleration component measured on 5 different frames along the deck of the ship. The vertical acceleration component, which is induced by the vertical bending mode, can be calculated by simply taking the average of the vertical acceleration of the two. The vertical acceleration induced by ship's vertical motions, such as heave and pitch, can be excluded easily by frequency filtering of the acceleration signal. Therefore, the

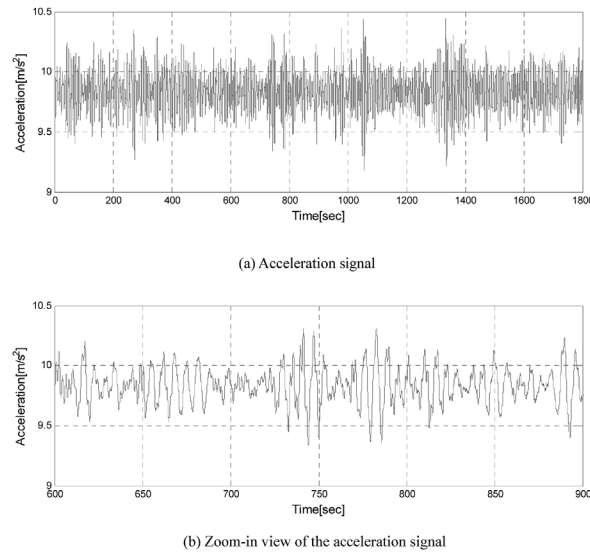


Fig. 9. Sample of the acceleration signal.

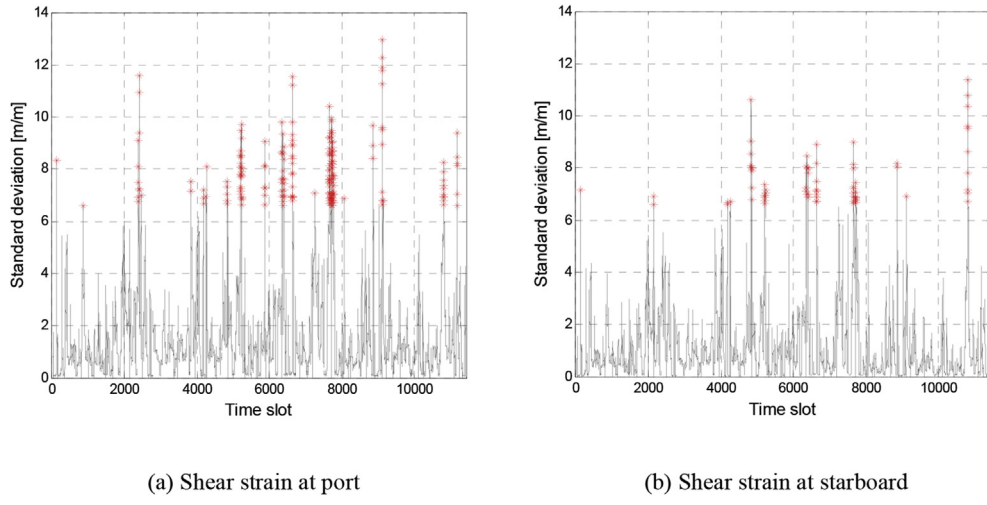


Fig. 10. Time-slot selection using the standard deviation of the shear strain.

vertical accelerations, a_v , at 5 frames, which were used to analyze the vertical bending mode are defined as Eq.(16).

$$a_v = \frac{a_{v, \text{port}} + a_{v, \text{star}}}{2} \quad (16)$$

where $a_{v, \text{port}}$ and $a_{v, \text{star}}$ stand for vertical acceleration at the port and starboard, respectively.

To analyze the torsional vibration mode, the rotational accelerations need to be extracted per frame. The rotational angular acceleration, a_θ , may be defined as the tangent of the two vertical acceleration components and can be simplified further as the difference between the two vertical accelerations normalized by the half breadth of the ship, as defined in Eq.(17).

$$a_\theta = \tan \frac{a_{v, \text{port}} - a_{v, \text{star}}}{B/2} \approx \frac{2(a_{v, \text{port}} - a_{v, \text{star}})}{B} \quad (17)$$

where B means the ship breadth.

6.2. Mode shapes and natural frequencies

Efforts have been made to identify the mode shapes of the vertical bending modes using the POD. As described previously, the vertical accelerations measured at 5 different locations along the ship length were used to construct the ensemble matrix, as expressed in Eq.(3), and the spatial coherence matrix, R , was then calculated. According to Eq.(10), the eigenvector of this spatial coherence matrix was assumed to be the vertical bending modes of the ship.

Fig. 11 presents the normalized 4 vertical acceleration mode shapes, which were derived from the 30 min. long data of the selected time-slots. The horizontal axis is the relative location of the accelerometer along the ship length, and the vertical axis is the vertical acceleration after normalization. The mode shapes were normalized so that the second norm of the modal vector is unity. Fig. 11(a) and (b) indicates two rigid body modes, the linear combination of which leads to both the heave and pitch modes. Fig. 11(c), (d) show the 2-node, 3-node vertical bending modes, respectively. The derived mode shapes are in line with the well-known vertical mode shapes of a slender structure. These acceleration mode shapes are identical to the displacement mode shapes because the displacement mode shapes can be achieved by integrating twice the acceleration mode shapes with respect to time.

Owing to the orthogonality of the mode shapes, the time evolution of the modal magnitude of an individual mode can be extracted easily provided that the modal decomposition is done successfully using the POD. This can be done by taking the inner product of both sides of Eq.(6) with the modal vector of interest. Fig. 12 shows the FFT results of the modal magnitude of four different modes shown in Fig. 11. The frequency contents of each mode were well represented by these FFT results, as shown in Fig. 12, and the natural frequencies of the 1st and 2nd vertical vibration modes is 0.54 and 1.08 Hz, respectively. The natural period of approximately 2 s. of 2-node vertical bending is the typical value of this size container carrier. Two rigid body modes, which combined the heave and pitch, have a peak around frequency value of 0.13 Hz. These rigid body modes also peak at the natural frequencies of both the 1st and 2nd vertical bending modes, which means that the 2 and 3-node vibration modes entails heave and pitch at these particular frequencies. The vibration modes also have small peaks at a low frequency range meaning that those modes have non-negligible quasi-static contribution.

The total 207 time-slots were processed and the derived modal parameters, such as the natural frequencies and mode shapes were analyzed further to check the variability of the quantities. Regarding the 3-node vertical bending, 196 time-slots were processed excluding 11 cases where the derived mode shapes were abnormal, which is believed to be due to the relatively small response magnitude. Fig. 13 shows the box and whisker plot of both 2 and 3-node vertical bending modes. The top and bottom of each box

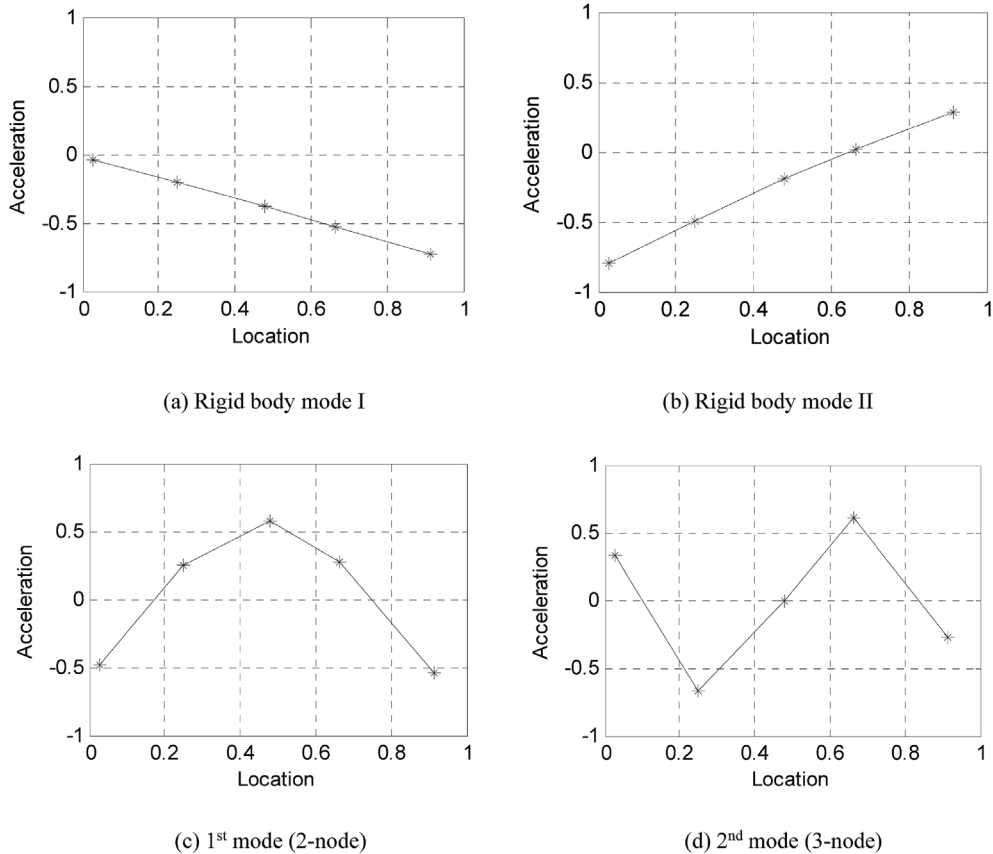


Fig. 11. Vertical acceleration mode shapes (at 21:54 of 2007/12/23).

indicate the mean values of the upper and lower 50% of the data, respectively. The upper and lower whiskers indicate the maximum and minimum values of the entire data set. The scatter of the mode shapes was not significant, which highlights the correctness of the analysis.

Fig. 14 shows the time evolution of the natural frequencies of both 2 and 3-node vertical bending modes. The time-slots of the horizontal axis are not continuous. Fig. 14(a) shows that the natural frequency of the 2-node vertical bending mode varies between 0.45 and 0.6 Hz depending on the time-slot. The change in natural frequency is considered to be induced by the different loading conditions, which unfortunately is not available information. Considering the general pattern of the wet natural frequency change, the ship is believed to be relatively unloaded during time-slots 30–60 and 100–180 because the natural frequencies in this time-slot range increased considerably compared to the others. A similar fluctuation pattern was observed for the natural frequency of the 3-node vertical bending mode, as shown in Fig. 14(b). For the 3-node vertical bending mode, the natural frequency varied between 0.9 and 1.15 Hz.

6.3. Damping ratios

The damping ratio is one of the most interesting dynamic modal parameters because it influences the absolute magnitude of the vibration directly, particularly near the resonance frequencies of the dominant vibration modes. The random decrement technique was used to extract the damping ratio of the 2-node vertical bending mode.

The original modal magnitude of the 2-node vertical bending mode was band-pass filtered for the succeeding process using the random decrement technique. Trapezoidal filter shown in Fig. 1 was used, where the filter parameters were set to $\omega_c = 0.5385$, $\Delta\omega_t = 0.07$, $\Delta\omega_S = 0.03$. ω_c was set to be the natural frequency of the 2-node vertical bending mode, whereas both $\Delta\omega_t$ and $\Delta\omega_S$ were chosen properly to cover the frequency component of the corresponding mode.

Fig. 15(a) shows the filtered time series of the modal magnitude along with the triggering points, which were used to select the ensembles for the conditional average. The level used to select the ensembles was set to be the standard deviation of the signal itself. The length of the ensemble was set to be N times of the natural period of the corresponding vibration mode. In this particular case, N was set to 15, so that about 15 vibration cycles were included in the free decay signal. Fig. 15(b) shows the evolution of the ensemble averages as the number of sample increases. The black solid lines are the interim free decay signal in the middle of the ensemble average and the red solid line is the converged one, which is considered to be the free decay signal of this particular vibration mode.

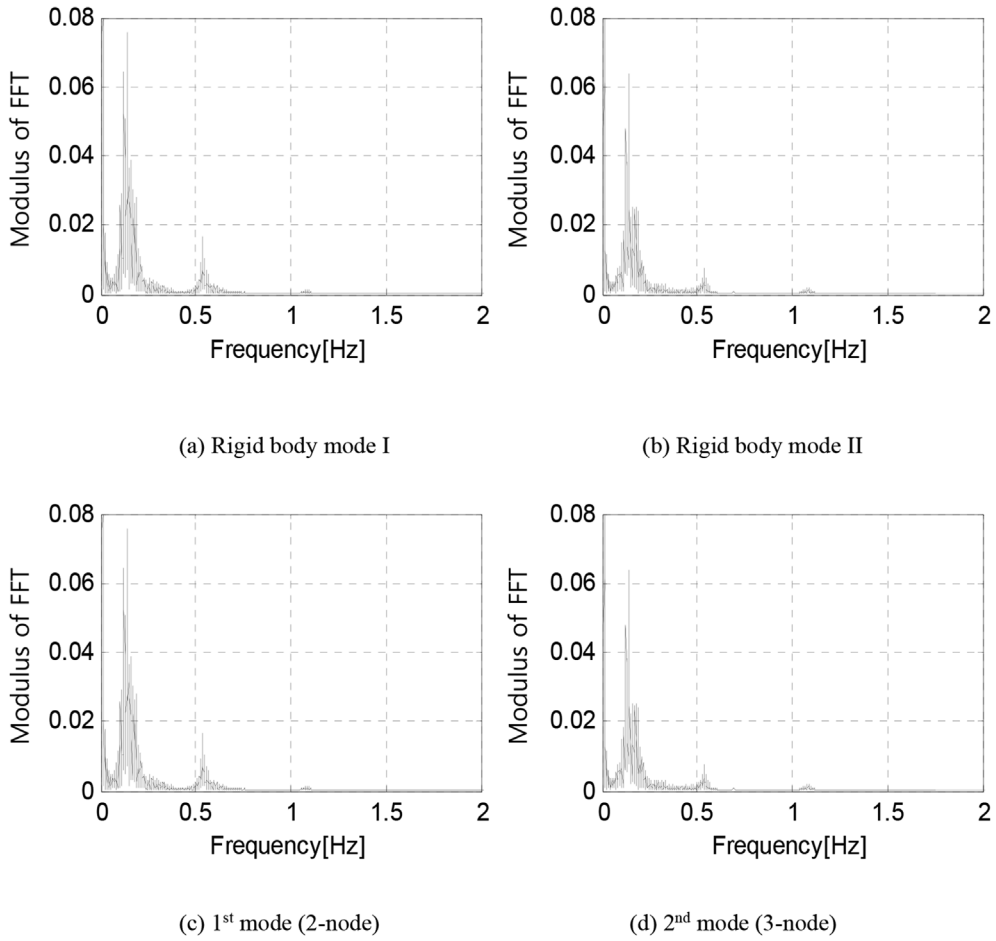


Fig. 12. FFT results of the vertical modal magnitude (at 21:54 of 2007/12/23).

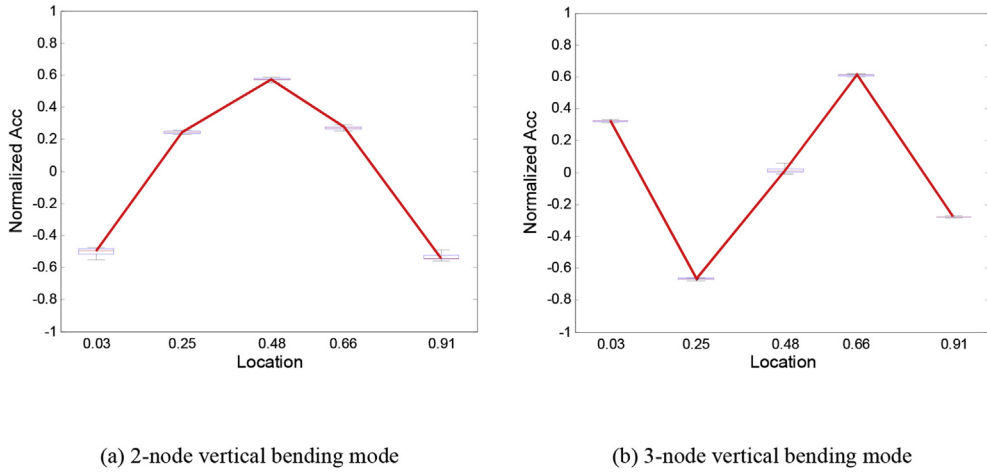


Fig. 13. Box and whisker plot of the mode shapes.

The damping ratio was calculated using the traditional logarithmic decrement, where local peaks of the free decay signal were fitted using a straight line after transforming the vertical axis to a log scale. Fig. 15(c) shows the local peaks along with its linear regression result. The damping ratio was derived using the slope of the straight line. The identified damping ratio of 2-node vertical bending mode in this particular time-slot was 1.33%, which is in the range widely accepted. The damping ratios derived from the other time-slots are presented in the following sections.

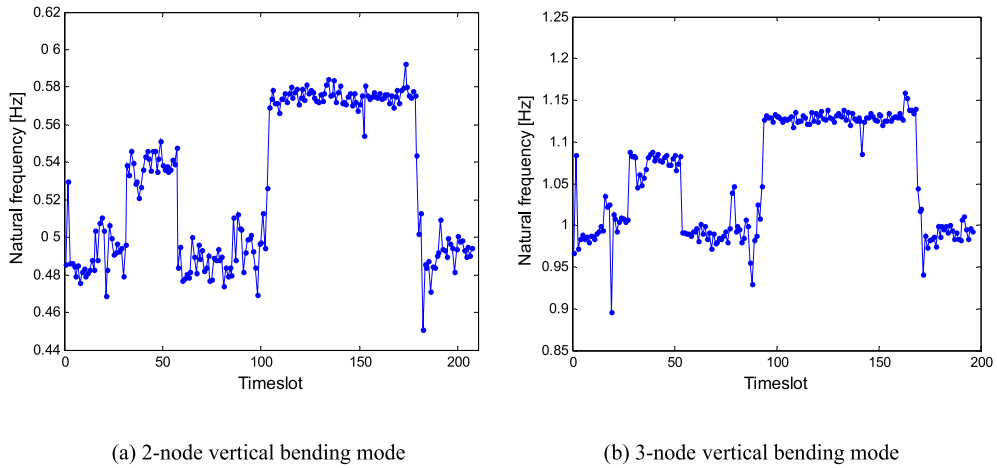


Fig. 14. Evolution of the natural frequencies.

The same analyses were performed for the 3-node vertical bending mode, where the only difference related to the analyses lies on the natural period of the vibration mode. A trapezoidal filter shown in Fig. 1 was used, where the filter parameters were set to $\omega_c = 1.0848$, $\Delta\omega_t = 0.07$, and

Fig. 16(a) shows the filtered time series of the modal magnitude along with the triggering points, which were used to select the ensembles for the conditional average. **Fig. 16(b)** shows the evolution of the ensemble averages as the number of sample increases. **Fig. 16(c)** shows the local peaks along with its linear regression result. The damping ratio of the 3-node vertical bending mode in this particular time-slot was found to be 1.74%, which is larger than that of the 2-node vertical bending mode. This trend is generally true

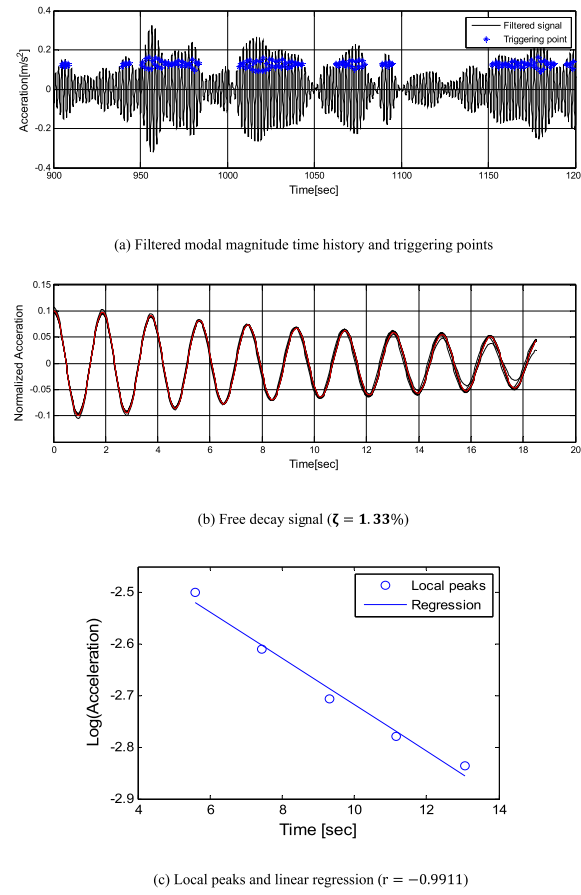


Fig. 15. Triggering points and free decay signal of the 2-node vertical mode (at 21:54 of 2007/12/23).

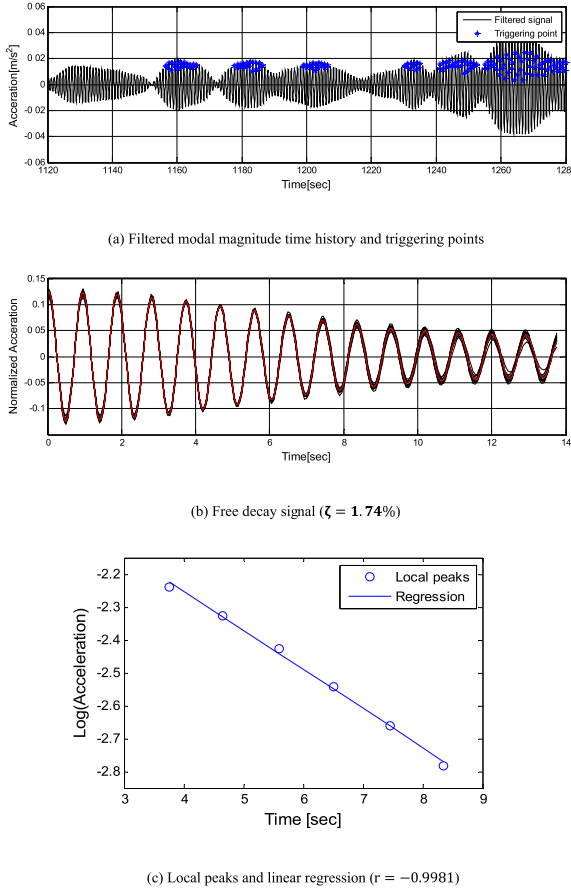


Fig. 16. Triggering points and free decay signal of the 3-node vertical mode (at 21:54 of 2007/12/23).

for all time-slots analyzed, which will be presented later.

Fig. 17 shows the time evolution of the damping ratio of both 2 and 3-node vertical bending modes. Fig. 17(a) and (b) confirms that the damping ratio of 2 and 3-node vertical bending modes varied between 1 and 4% and 1–3%, respectively. A comparison of the time fluctuation pattern of natural frequency and damping ratio showed that both quantities are inversely proportional to each other. Considering the inference regarding the loading condition with respect to the change in natural frequency, it may be deduced that the damping ratio decreases as the ship is less loaded. This is in line with the popular speculation that the majority of damping in the container vessel is induced by friction between the containers and its supporting structures.

Fig. 18 shows correlation plot between the natural frequency and damping ratio derived for the selected time slots. Bar charts show probability distribution of both natural frequencies and damping ratios. Although the correlation was not strong, an inverse proportionality was observed between the two parameters, which means that damping becomes larger when the natural frequency becomes smaller, supporting the above-mentioned statement regarding the relationship between the loading condition and damping.

7. Strains and fatigue damages

7.1. Strain correlation

To determine if the vessel is exposed to vertical bending or torsion, the correlation between the shear strain and deck normal strain were investigated. Fig. 19 shows the deck normal strain pattern depending on the vibration mode that the vessel is exposed to.

Before the correlation plot, two normal strains at the deck was added and subtracted to form the additional variables. One is called the ‘Sum_deck’, which is the summed normal strains of both port($PsHi$) and starboard($SbHi$), and the other is called ‘Diff_deck’, which is defined as the difference in the normal strains at the deck, both of which are defined as Eq.(18). ‘Sum_deck’ is an indicator of vertical bending mode and Diff_deck is that of the torsion or horizontal bending mode. Therefore, correlation of these quantities with the shear strain at the mid-height becomes a good indicator of the presence of vertical bending or torsion.

$$\begin{aligned} \text{Sum_deck}(t) &= PsHi(t) + SbHi(t) \\ \text{Diff_deck}(t) &= PsHi(t) - SbHi(t) \end{aligned} \quad (18)$$

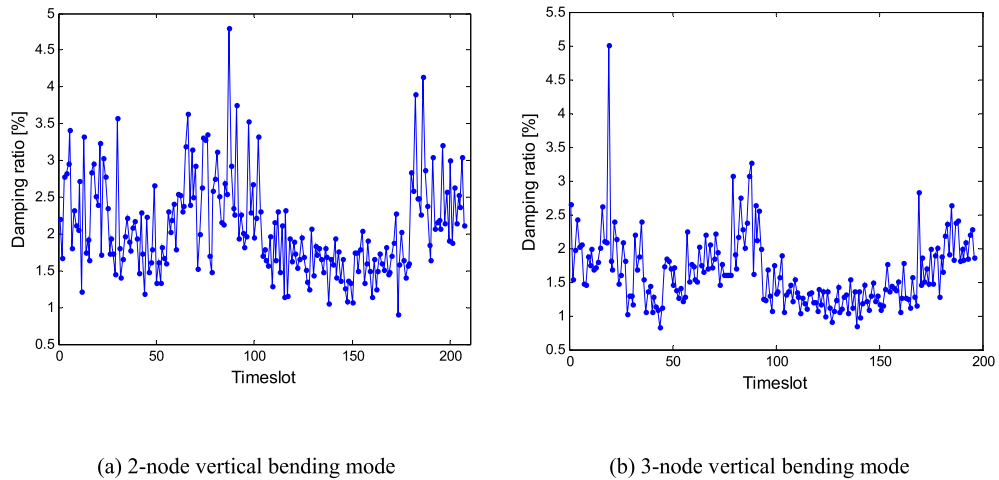


Fig. 17. Evolution of the damping ratios.

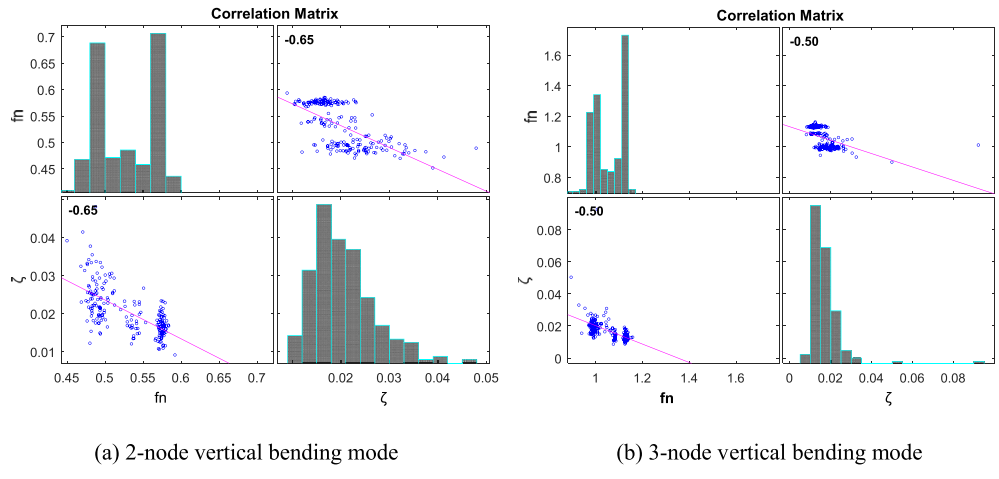


Fig. 18. Correlation matrix between the natural frequency and damping ratio.

Because all these correlations are expected to be valid only for the vibration component, deck normal strain and shear strain at the mid-height were filtered using the same filter parameters. Fig. 20 shows the correlation plot between the shear strains at the mid-height of vessel and normal strains on deck of cargo hold 8. Fig. 20(a) and (c) shows that there is a very strong positive correlation between the shear strain and ‘Sum_deck’ strain, which proves that the shear strain at the mid-height of the vessel is induced by vertical bending. On the other hand, Fig. 20(a) and (c) shows that there is almost no correlation between the shear strain and ‘Diff_deck’ strain, which suggests that the shear strain at the mid-height of vessel has nothing to do with torsion or horizontal bending.

The correlation plot shown in Fig. 20 was generally true for almost all selected time-slots, as shown in Fig. 21 in terms of the correlation coefficients between the shear strain and 'Sum_deck' or 'Diff_deck' strain. The absolute values of the correlation coefficients between the shear strain and 'Diff_deck' strain were higher for a few time-slots, and those between the shear strain and 'Sum_deck' strain were higher at the same time-slots.

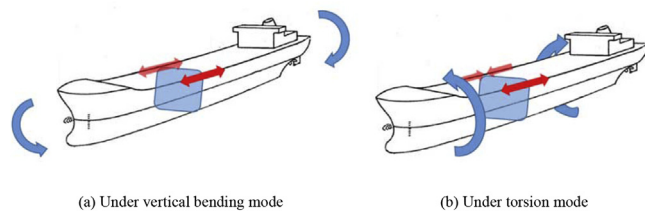


Fig. 19. Deck normal strain according to the vibration mode.

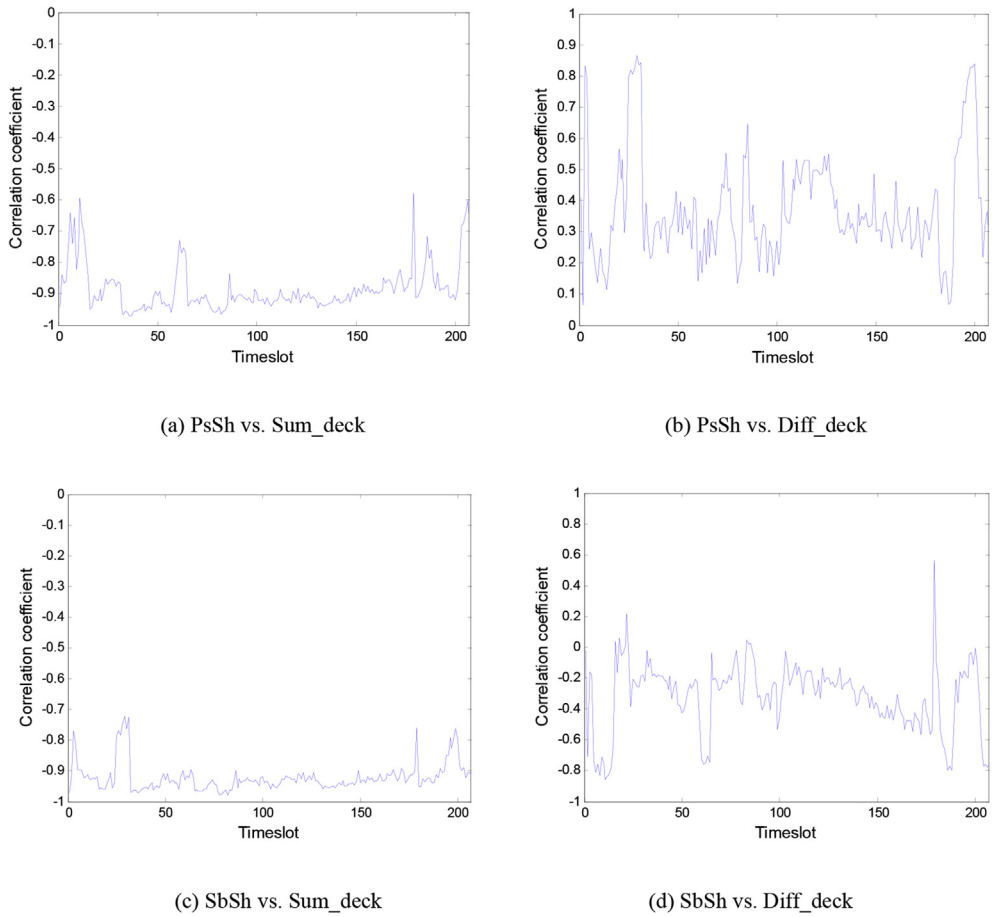


Fig. 20. Correlation plot of the shear and deck strain at cargo hold 8 (at 19:49 of 2008/03/16).

7.2. Strain vs. modal magnitude

Efforts have been made to examine the correlation between the LBSG data and the acceleration modal magnitude. The idea starts from the speculation that the acceleration modal magnitude of the 2-node vertical bending mode must be proportional to the strains measured at the mid-ship section of the vessel.

For a better comparison, the time series was filtered to the vibration and wave frequency component by applying a high and low pass filter. For the vibration frequency component, the filtering parameters were set to $\omega_c = 0.5385$, $\Delta\omega_t = 0.025$, and $\Delta\omega_S = 0.03$, and for the wave frequency component, they were set to $\omega_c = 0.155$, $\Delta\omega_t = 0.095$, and $\Delta\omega_S = 0.05$.

Fig. 22(a) compares the filtered time series of the modal magnitude and deck strain for the vibration frequency component. For comparison, two filtered signals were normalized in such a way that the length of the signal becomes unity. Fig. 22(a) shows a strong correlation between the two signals, except for the phase lag. The observed phase lag, 99.23°, between the two signals was unexpected and may be due to the failure of synchronization between the acceleration sensor and LBSG. The phase lag was observed in the other time-slots, but with different magnitudes. Fig. 22(b) compares those of the wave frequency component. The modal magnitude and strain measured at the deck did not match each other as perfectly as the case of the vibration frequency case but the fluctuation pattern of the two signals is similar to each other. This fact is not surprising because, in the wave frequency range, the structural response is of quasi static nature and cannot be accurately described by few structural natural modes only. Indeed, when the response is quasi static the representation of the response in terms of a series of natural modes is not practical because a very large number of modes is necessary in order to ensure proper convergence.

Fig. 23(a) shows the correlation plot between the acceleration modal magnitude and deck strain of the mid-ship deck for the vibration frequency component, where the phase lag was removed artificially. As expected, the correlation between the two physical quantities was quite strong. This strong correlation between the modal magnitude and deck strain was true for all time slots selected, as shown in Fig. 23(b).

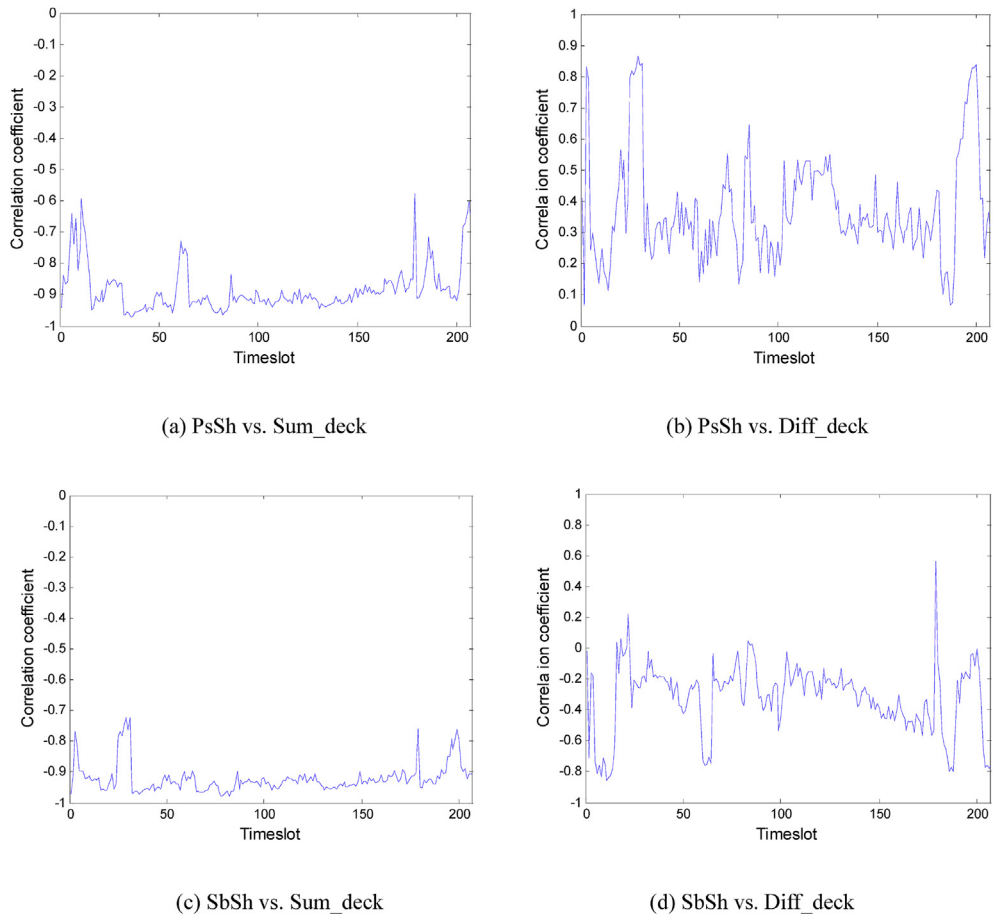


Fig. 21. Correlation coefficients between the shear and deck strain amid ship.

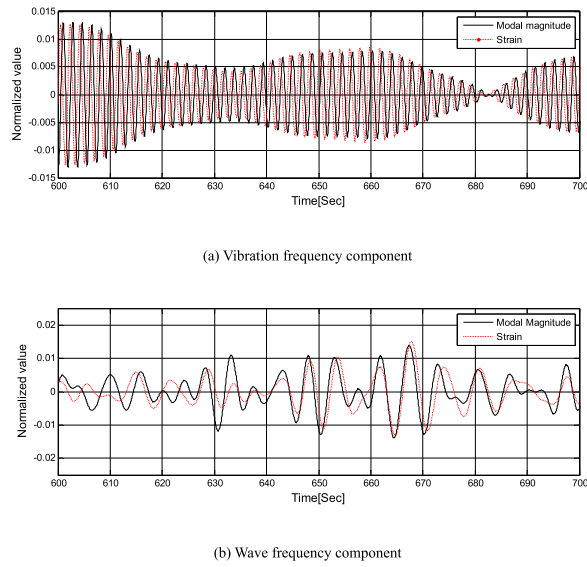


Fig. 22. Comparison of the filtered time histories of the modal magnitude and deck strain (at 21:54/2007/12/23).

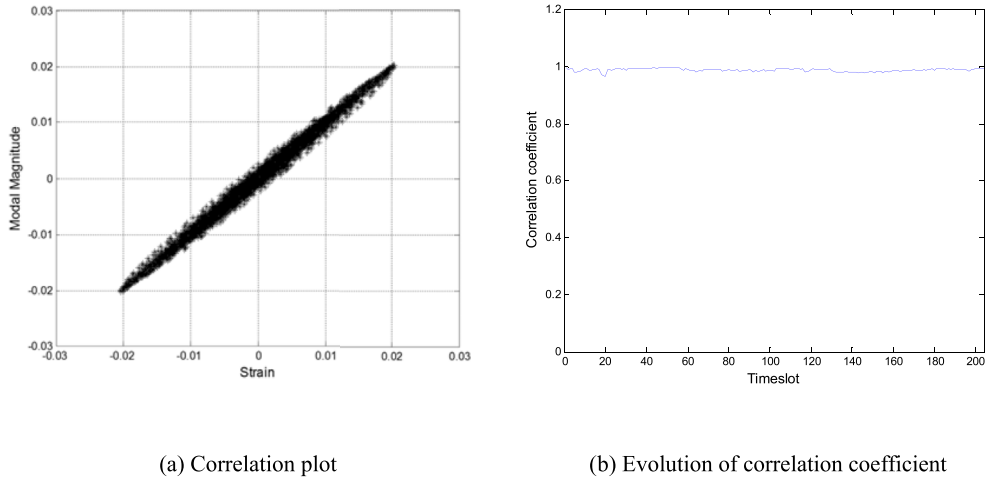


Fig. 23. Correlation between the modal magnitude and deck strain ($r = 0.9964$, at 21:54/2007/12/23).

7.3. Fatigue damage

Fig. 24 shows the stress time histories at the deck of the midship: one with a vibration component and the other one without a vibration component. The stress was calculated by simply multiplying the Young's modulus by the measured strain. The stress time histories without vibration were obtained by applying a low-pass filter to the original signal with a cut-off frequency of 0.4 Hz. The peak stresses tended to level down by some amount when the vibration component was removed from the original signal.

Owing to the wide-band nature of the response spectrum, the direct rainflow counting method, which is considered to be the standard cycle counting method, was used for cycle counting [22]. Once the probability distribution of the stress range is obtained using the direct cycle counting method, it will be combined with the SN curve and the fatigue damage was estimated under the assumption of the linear accumulation theory, which was realized using Palmgren-Miner's rule.

To calculate the fatigue damage, a certain virtual local geometry, which contains the structural discontinuity was assumed with a stress concentration factor of 2.0. Assuming that the SCF transfers the measured stress at the deck into the local hot spot stress, a unified SN curve, which is based upon the hot spot stress was used. The SN curve was defined, as shown in Eq.(19).

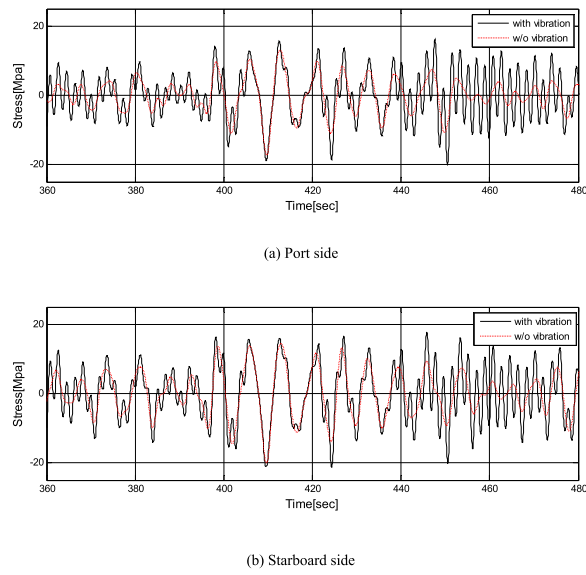


Fig. 24. Stress time histories with and without vibrations on the deck of the cargo hold 6.

Table 3

SN parameters for air or with cathodic protection.

S-N curve	Material	$N \leq 10^7$		$N > 10^7$	
		$\log \bar{a}$	m	$\log \bar{a}$	m
I	Welded joint	12.164	3.0	15.606	5.0
III	Base Material	15.117	4.0	17.146	5.0

$$\log N = \log \bar{a} - m \log \Delta\sigma$$

N=Predicted number of cycles to failure for stress range $\Delta\sigma$

$\Delta\sigma$ =Stress range

m=Negative inverse slope of S–N curve

$$\log \bar{a} = \text{Intercept of log } N\text{--axis by S--N curve}$$

(19)

The hot spot stress based SN curve specified in DNV CN30.7 [21] was used for the fatigue damage evaluation; Table 3 lists the parameters of the SN curve.

The Palmgren-Miner rule allows one to calculate the accumulated fatigue damage caused by randomly fluctuating stress cycles. The basic assumption behind it is that the total accumulated fatigue damage induced by irregular stress cycles can be obtained by a linear superposition of the fatigue damage caused by the constant amplitude stress cycles.

$$D = \sum_{i=1}^k \frac{n_i}{N_i} \quad (20)$$

where n_i means the number of stress cycles estimated using the rainflow counting method and N_i is the number of cycles that lead to fatigue failure under the corresponding constant amplitude stress cycle. k is the number of stress blocks of a constant amplitude. Fatigue failure is considered to be present in the structure when the superimposed fatigue damage, D , reaches unity.

Short-term fatigue damage for the 207 sea states selected were calculated using the assumed SCF of 2.0 according to the above-mentioned procedure. Fig. 25 and Fig. 26 show the time evolution of the short-term fatigue damage at both the port and starboard side of the deck, at cargo holds 6 and 8, respectively. In all four cases, the short-term fatigue damage was leveled out by a certain amount when the vibration frequency component was removed in the fatigue damage calculation. The relative portion of the wave frequency response from the fatigue damage point of view depends on the absolute magnitude of fatigue damage. When the focus is given to the case of the largest short-term fatigue damage, fatigue damage without a vibration component was approximately 60% of that with a vibration. Note that the relative portion of fatigue damage together with the damage itself depends on the assumed SCF due to the cubic power relationship between the stress range and fatigue life. In addition, the short-term fatigue damage at the port and starboard side showed a similar trend and the fatigue damage at cargo hold 6, which is located closer to the mid-ship was larger than that at cargo hold 8.

The fatigue damage for the entire time span during the measurement campaign, which lasted for approximately 10 months, was calculated and the expected 20 years fatigue damage was estimated by a simple extension of the calculated fatigue damage. Fig. 27 shows a bar chart of the calculated 10-months fatigue damage at four different locations. The relative portion of fatigue damage at

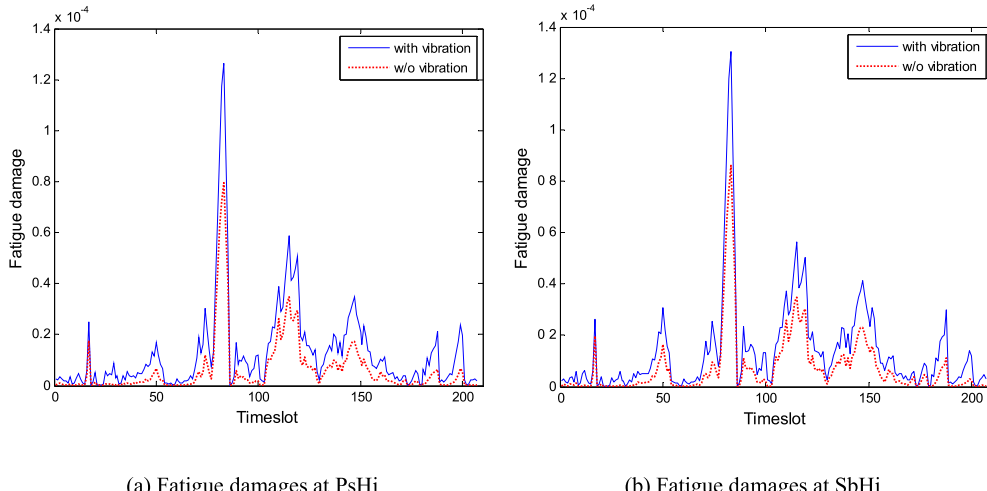


Fig. 25. Short-term fatigue damage at the deck of cargo hold 6.

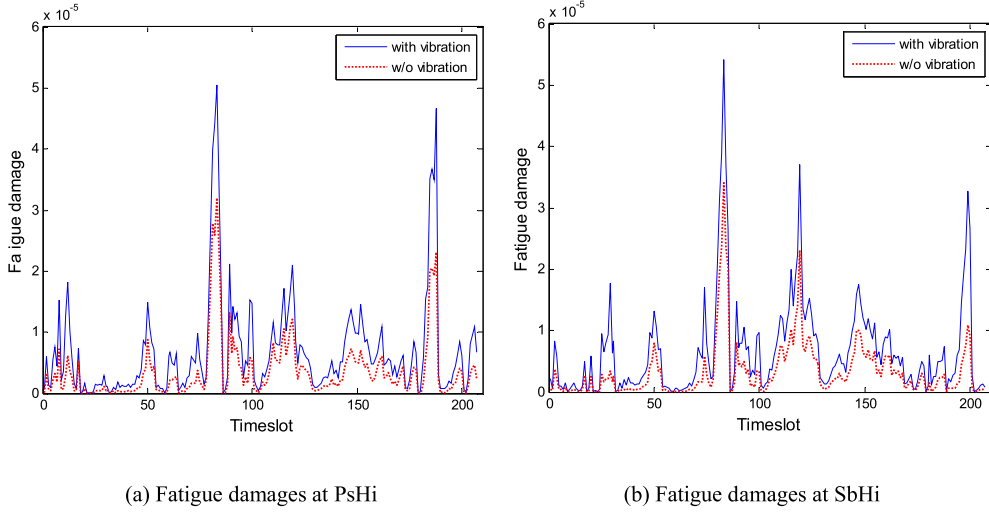


Fig. 26. Short-term fatigue damages at the deck of cargo hold 8.

cargo hold 6, when vibrations were not considered was approximately 56%. In the case of cargo hold 8, it was slightly larger than 56%, reaching approximately 60%. As suggested above, the fatigue damage at the deck of cargo hold 6 was larger than that of cargo hold 8 because of the closer distance to the center of the ship. In addition, the fatigue damage at both the port and starboard were similar.

Table 4 lists the expected 20-year fatigue damage, which was calculated by multiplying a factor of 24 to the 10-months fatigue damage. The largest expected 20-year fatigue damage was 0.174 at the deck of H6, which falls in the safe side from a fatigue strength point of view. The fatigue damage increased from 0.102 to 0.174 for SbHi, which corresponds to approximately 70% in terms of the increase rate.

Expected fatigue life and the vibration contribution obtained from the full scale measurement data of studied vessel can be compared with a reference vessel studied by Ref. [10]. Barhoumi and Storhaug(2014) found that the expected fatigue life of 8600TEU container carrier voyaged between Europe and Asia was about 50 years under the assumption of 2.0 stress concentration factor. This is about half of studied vessel and the discrepancy may be attributed to the long measurement period of reference vessel, which is 4 years. On the other hand, the damage contribution of vibration in the reference vessel was about 57%, and this is not far from that of studied vessel, which is 46%.

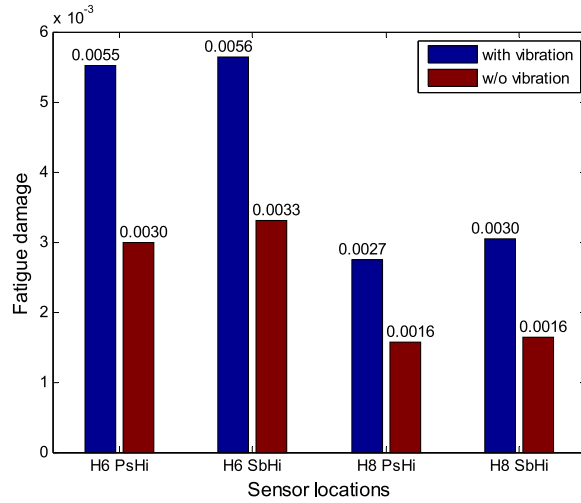


Fig. 27. Fatigue damage for the entire measurement period.

Table 4
Expected 20 year fatigue damage.

	With vibration	Without vibration	$100*(D_{w\ vib} - D_{wo\ vib})/D_{wo\ vib}$
H6 PsHi	0.170	0.092	85%
H6 SbHi	0.174	0.102	70%
H8 PsHi	0.084	0.049	74%
H8 SbHi	0.094	0.051	86%

8. Conclusions

Based upon the study carried out in this study, the following conclusions were made:

- The vibration modes were extracted successfully by the POD using the vertical acceleration measured along the vessel and the modal responses were decomposed into 4 different modes. The corresponding natural frequencies were derived by taking a Fourier transform of the derived time series of the modal magnitude.
- The natural frequency of the 2 node vertical bending mode changed from 0.45 to 0.6 Hz during the measurement period and the fluctuations of the natural frequency depended on the loading condition of the vessel. In the case of the 3 node vertical bending mode, fluctuations took place between 0.9 and 1.15 Hz with a similar temporal trend as in 2 node case.
- The free decay signals of modal magnitude were derived successfully by RDT, and the damping ratios were derived using a logarithmic decrement technique. The damping ratio of the 2 node vertical bending mode varied from 1% to 3% depending on the loading condition, and a similar pattern was observed for the 3 node vertical bending mode.
- The correlation between the shear strain at the mid-height of the vessel and deck normal strain was studied to check the presence of the torsional response during the measurement period. The shear strain has a strong correlation with the summation of the port and starboard strain, which means that the shear strain was induced by vertical bending rather than torsion.
- A strong correlation was observed between the acceleration-based modal magnitude and the strain on deck in the vibration regime. This means that the acceleration-based vibration mode may be used to derive the local strain, wherever the location is, provided that the modal strain is given. The correlation between the acceleration-based modal magnitude and strain on deck in the wave frequency regime was quite weak, and is suspected to be caused by the local deformation effect.
- Fatigue damage at an artificial typical structural detail on deck was estimated with or without vibration, and the fatigue damage was increased by approximately 70–85% due to vibrations, particularly the vertical bending mode. The expected fatigue damage for a service life of 20 years was approximately 0.17, which is still far less than 1.0.

Acknowledgement

Authors acknowledge the permission of CMA-CGM to use the measured data for the present analyses. S. Malenica acknowledges the support from a National Research Foundation of Korea grant funded by the Korean Government (MSIP) through GCRC-SOP (Grant No. 2011-0030013).

References

- [1] Remy F, Molin B, Ledoux A. Experimental and numerical study of the wave response of a flexible barge. Proceedings of the 4th international conference on hydroelasticity in marine technology, Wuxi, China. 2006.
- [2] Iijima K, Hermundstad OA, Zhu S, Moan T. Symmetric and antisymmetric vibrations of a hydroelastically scaled model. Proceedings of the 5th international conference on hydroelasticity in marine technology, Southampton, UK. 2009.
- [3] Miyake R, Matsumoto T, Zhu T, Usami A, Dobashi H. Experimental studies on the hydroelastic response using a flexible mega-container ship model. Proceedings of the 5th international conference on hydroelasticity in marine technology, Southampton, UK. 2009.
- [4] Oka M, Oka S, Ogawa Y. An experimental study on wave loads of a large container ship and its hydroelastic vibration. Proceedings of the 5th international conference on hydroelasticity in marine technology, Southampton, UK. 2009.
- [5] Hong S, Kim BW, Nam BW. Experimental study on torsion springing and whipping of a large container ship. Proceedings of the 21st international offshore and polar engineering conference, Maui, Hawaii, USA, June, 2011.
- [6] Hirdaris SE, Bakkers N, White N, Temarel P. Service factor assessment of a great lakes bulk Carrier incorporating the effects of hydroelasticity. Mar Technol 2009;46(2):116–21.
- [7] Miyake R, Matsumoto T, Yamamoto N, Toyoda K. On the estimation of hydroelastic response acting on an ultra-large container ship. Proceedings of the 20th international offshore and polar engineering conference, Beijing, China. 2010.
- [8] Drummelen I, Wu MK, Moan T. Experimental and numerical study of containership responses in severe head seas. Mar Struct 2009;22:172–93.
- [9] Jensen JJ. Stochastic procedures for extreme wave load predictions – wave bending moment in ships. Mar Struct 2009;22(2):194–208.
- [10] Barhoumi M, Storhaug G. Assessment of whipping and springing on a large container vessel. International Journal of Naval Architecture and Ocean Engineering 2014;6:442–58.
- [11] Storhaug G. The measured contribution of whipping and springing on the fatigue and extreme loading of container vessels. International Journal of Naval Architecture and Ocean Engineering 2014;6:1096–110.
- [12] Lumley. Stochastic tools in turbulence. New York: Academic Press; 1970.
- [13] Feeny BF, Kappagantu R. On the physical interpretation of proper orthogonal modes in vibrations. J Sound Vib 1998;211:607–16.
- [14] Feeny BF. On proper orthogonal coordinates as indicators of modal activity. J Sound Vib 2002;255:805–17.
- [15] Cole HA. On-the-line analysis of random vibrations. AIAA Paper No 1968:68–288.
- [16] Cole HA. Method and Apparatus for Measuring the Damping Characteristics of a Structure. 1971. United States Patent No.3, 620,069, Nov.16.

- [17] Ibrahim SR, Mikulcik EC. A method for the direct identification of vibration parameter from the free response. Shock and Vibration Bulletin 1977;47(4):183–98.
- [18] Mariani R, Dessi D. Analysis of the global bending modes of a floating structure using the proper orthogonal decomposition. J Fluid Struct 2012;28:115–34.
- [19] Kim Y, Park SG. Wet damping estimation of the scaled segmented hull model using the random decrement technique. Ocean Eng 2014;75:71–80.
- [20] Kim Y, Ahn IG, Park SG. Extraction of the mode shapes of a segmented ship model with a hydroelastic response. International Journal of Naval Architecture and Ocean Engineering 2015;7:979–94.
- [21] DNV. Fatigue assessment of ship structures. Classification notes No.30.7. 2010.
- [22] ASTM. Standard practices for cycle counting in fatigue analysis, Annual Book of ASTM Standards Vol. 03.01. 1997. designation E1049-85. USA.